Distinct speed dependence of entorhinal island and ocean cells, including respective grid cells

Chen Sun[a,b,c,1], Takashi Kitamura[a,b,c,1], Jun Yamamoto[a,b,c], Jared Martin[a,b,c], Michele Pignatelli[a,b,c], Lacey J. Kitch[d], Mark J. Schnitzer[d,e,f], and Susumu Tonegawa[a,b,c,g,2]

[a]RIKEN–Massachusetts Institute of Technology Center for Neural Circuit Genetics, Picower Institute for Learning and Memory, Massachusetts Institute of Technology, Cambridge, MA 02139; [b]Department of Biology, Massachusetts Institute of Technology, Cambridge, MA 02139; [c]Department of Brain and Cognitive Sciences, Massachusetts Institute of Technology, Cambridge, MA 02139; [d]James H. Clark Center, Stanford University, Stanford, CA 94305; [e]Cracking the Neural Code Program, Stanford University, Stanford, CA 94305; [f]Howard Hughes Medical Institute, Stanford University, Stanford, CA 94305; and [g]Howard Hughes Medical Institute, Massachusetts Institute of Technology, Cambridge, MA 02139

Contributed by Susumu Tonegawa, June 15, 2015 (sent for review June 2, 2015)

Entorhinal–hippocampal circuits in the mammalian brain are crucial for an animal's spatial and episodic experience, but the neural basis for different spatial computations remain unknown. Medial entorhinal cortex layer II contains pyramidal island and stellate ocean cells. Here, we performed cell type-specific Ca^{2+} imaging in freely exploring mice using cellular markers and a miniature head-mounted fluorescence microscope. We found that both oceans and islands contain grid cells in similar proportions, but island cell activity, including activity in a proportion of grid cells, is significantly more speed modulated than ocean cell activity. We speculate that this differential property reflects island cells' and ocean cells' contribution to different downstream functions: island cells may contribute more to spatial path integration, whereas ocean cells may facilitate contextual representation in downstream circuits.

speed | grid cell | calcium imaging | entorhinal | hippocampus

Entorhinal–hippocampal neuronal circuits are crucial for spatial and contextual representation, navigation, and episodic memory (1, 2). In the entorhinal cortex (EC), grid cells (3), which have hexagonal periodicity of their spatial firing pattern, are most strongly represented in layer II of the medial entorhinal cortex (MECII) (4). These, and other spatially modulated cells in EC, as well as place cells in hippocampus, are thought to together underlie the brain's "GPS" in spatial functions.

Recently, in EC layer II, we and other groups have identified two different types of excitatory neurons populations. Hexagonally arranged clusters (islands) composed of CalbindinD-28K (Calbindin) and Wolfram syndrome 1 (Wfs1)-positive pyramidal cells (island cells; 40%) are surrounded by Reelin-positive stellate cells (ocean cells; 60%) (5–7). Whereas ocean cells project to the dentate gyrus (DG) and CA3, island cells project to both CA1 inhibitory interneurons, as well as (weakly) to the CA1 excitatory cells (5).

Given this clear morphological, genetic, and anatomical dichotomy of ECII excitatory cells, we wondered whether they differ in their activity patterns. To date, few studies have investigated the relationship between anatomy and spatial coding in EC; thus, there is very little known about how ocean cells and island cells differ in their coding of space. In previous literature, it has been suggested that specific types of spatially modulated cells, particularly grid cells, may be differentially contributed by the two cell types; however, this remains controversial in the literature (8, 9) owing to the difficulty of directly monitoring island and ocean cells during behavior. Here, we are able to selectively monitor the Ca^{2+} dynamics of either island or ocean cells in freely exploring mice and, in doing so, resolve whether both populations contain grid cells and, if so, whether their spatial coding properties differ or not. A dichotomy of activity properties in island and ocean cells gives insight into how different downstream spatial functions in hippocampus arise.

Results

To study ocean cells, we make use of the fluorescent calcium sensor GCaMP6f (10). We injected retrogradely transported adenoassociated virus (AAV)2/5-Syn-GCaMP6f virus into the dorsal DG of WT C57BL6 mice (Fig. 1*A*). Because ocean cells but not island cells project to the DG (5), GCaMP6f expression in the MEC was restricted to the Reelin-positive ocean cell populations (Fig. 1*C* and Fig. S1). To study island cells, we injected AAV2/5-Syn-DIO-GCaMP6f virus into the superficial layer of MEC of Wfs1-Cre transgenic mice (5) (Fig. 1*B*). Because Cre expression in the EC of these mice is specific for island cells (5), GCaMP6f expression in the MEC was restricted to the Calbindin/Wfs1-positive island cells (Fig. 1*D* and Fig. S1). For both cohorts of mice, we implanted a microendoscope probe (11) into dorsal MEC and performed Ca^{2+} imaging using a miniaturized, head-mounted fluorescence microscope as the mice freely explored a square arena (100 × 100 cm) (Fig. 1 *E* and *F*). We monitored somatic Ca^{2+} dynamics in three Ocean-GCaMP6f mice (177, 180, and 198 = 555 cells in total) and three Island-GCaMP6f mice (196, 196, and 199 = 591 cells in total), as each animal ran freely for 90 min in a familiar open field (Fig. 1 *E–H*). Post hoc analyses confirmed that imaging occurred in dorsal MEC of all ocean and island mice based on stereotaxic coordinates (Fig. 1*I* and Fig. S2), that the MEC laminar structure and hippocampal structure were preserved (Fig. 1*J* and Fig. S2), that cholinergic inputs into the MEC were preserved (Fig. S3), and that there was no inflammation reaction in the dorsal MEC regions (Fig. 1 *J* and *K*, and Fig. S3).

Both ocean and island mice had neurons with a spatially periodic Ca^{2+} event pattern during exploration (Fig. 2 *A* and *B*, and Fig. S4)

Significance

The importance of entorhinal–hippocampal circuits in the mammalian brain for an animal's spatial and episodic experience is known, but the neural basis for these different spatial computations is unclear. Medial entorhinal cortex layer II contains island and ocean cells that project via separate pathways into hippocampus. We performed Ca^{2+} imaging in freely exploring mice using cellular markers and a miniature head-mounted fluorescence microscope, the first time (to our knowledge) in entorhinal cortex. We found that, although both oceans and islands contain grid cells, islands are significantly more speed modulated than oceans. We speculate that this differential property reflects islands' and oceans' contribution to different downstream functions.

Author contributions: C.S., T.K., J.Y., and S.T. designed research; C.S., T.K., J.M., and M.P. performed research; C.S., T.K., J.Y., M.P., L.J.K., M.J.S., and S.T. analyzed data; and C.S., T.K., L.J.K., M.J.S., and S.T. wrote the paper.

The authors declare no conflict of interest.

Freely available online through the PNAS open access option.

[1]C.S. and T.K. contributed equally to this work.

[2]To whom correspondence should be addressed. Email: tonegawa@mit.edu.

This article contains supporting information online at www.pnas.org/lookup/suppl/doi:10.1073/pnas.1511668112/-/DCSupplemental.

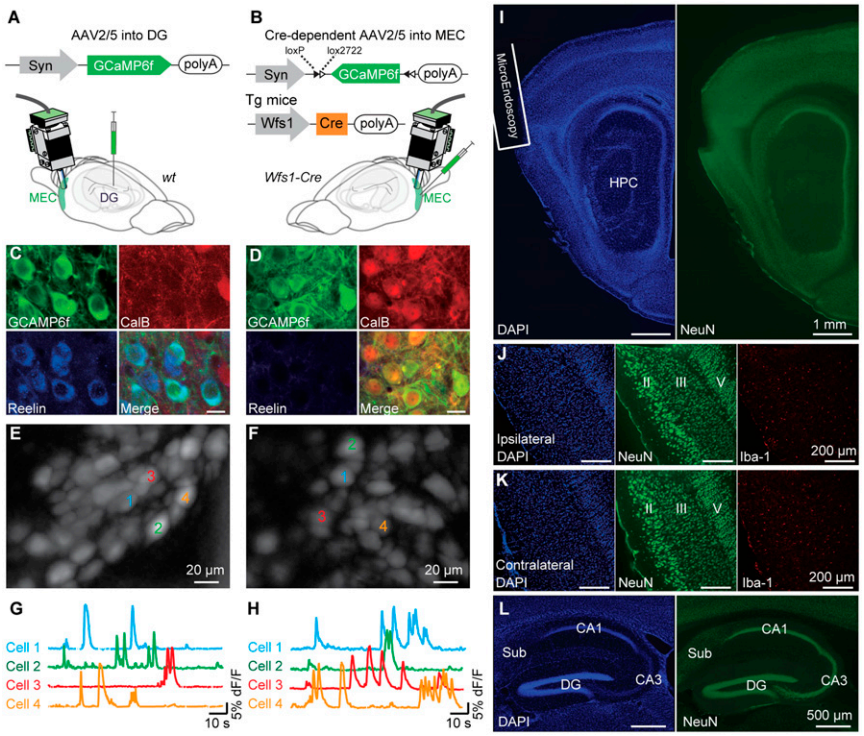

Fig. 1. Specific labeling of ocean cells and island cells by GCaMP6f. (*A*) Labeling method of ocean cells by GCaMP6f. Injection of AAV2/5-Syn-GCaMP-6f into DG of WT mice and implantation of the microendoscope into MEC. (*B*) Labeling method of island cells by GCAMP6f. Injection of AAV2/5-Syn-DIO-GCaMP-6f into MEC and implantation of the microendoscope into MEC. (*C* and *D*) Parasagittal sections of EC visualized with GCaMP6f-labeled ocean cells (*C*) and island cells (*D*) (green) and immunostained with anti-Reelin (blue) and anti-CalB (red). (*E* and *F*) Stacked image of imaging from field in MEC of ocean cells (*E*) and island cells (*F*) through the microendoscope. (*G* and *H*) Relative fluorescence changes ($\Delta F/F$) for four ocean cells and island cells. (*I*) Parasagittal sections of MEC of microendoscopy implanted animal immunostained with anti-NeuN (green) and DAPI (blue). (*J* and *K*) Ipsilateral (*J*) and contralateral side (*K*) of parasagittal sections of dorsal MEC of microendoscopy implanted animal immunostained with anti-NeuN (green), anti–Iba-1 (red), and DAPI (blue). (*L*) Ipsilateral side of parasagittal sections of dorsal hippocampus of implanted animal immunostained with anti-NeuN (green) and DAPI (blue).

that resembled grid firing patterns seen from neuronal spiking. Oceans and islands also contained spatial cells (Fig. 2 *C* and *D*, and Fig. S5)—cells whose activation patterns encoded statistically significant spatial information about the mouse's location in the arena (*Materials and Methods*). We define a grid cell based on calcium events analogous to grid cells defined based on neuronal spiking and observed that island and ocean cells had no difference in grid score distribution (Fig. 2*E*) ($P = 0.58$, Kolmogorov–Smirnov test). We determined the proportion of neurons with a gridness score significantly above chance levels in both groups of mice (Fig. 2*F* and *Materials and Methods*) and found no difference in the proportion of grid cells in islands and oceans (Fig. 2*F*; $P = 0.92$, χ^2 test). We further evaluated the robustness of calcium-detected grid cells by studying the orientation (Fig. 2*G* and *Materials and Methods*) and the spacing (Fig. 2*H* and *Materials and Methods*) of the observed grid cells, and found that the grid cells showed (*i*) a mean spatial orientation of 8.27° to the borders and (*ii*) discrete grid spacing (with peaks at 49, 71 cm, for a ratio of 1.45), both of which resemble known properties of grid cells based on neuronal spikes (12–14).

We next sought a functional difference between island and ocean cells. We observed that more island cells tend to be active when the animal is running fast compared with slow, whereas ocean cells do not show this tendency as much (Fig. 3*C*) (Fig. 3 *A* and *B*, example traces of ocean and island animal behavior, with cell activity raster plots). To quantify this, we calculated the correlation between normalized population activity and normalized animal speed, across all animals (*Materials and Methods* and Fig. S6) for both island and ocean populations and found that the percentage of island cells active was correlated with animal speed (Pearson correlation coefficient = 0.63, $P < 10^{-50}$), whereas this correlation was significantly lower for ocean cells (Pearson correlation coefficient = 0.27, $P < 10^{-50}$; Fisher *r*-to-*z* transform: $P < 10^{-50}$, $z = 36.9$).

To examine the speed modulation of single cells, we determined the correlation between the rate of calcium transients and animal speed for each cell (*Materials and Methods*). Regression analyses showed positive correlations in nearly all entorhinal cells (972/1,142 cells = 85%; Fig. 3*D*), confirming a known property of MEC cells in general (4, 15). However, when the cell type identity of each individual cell is taken into account, we noticed that island cells had steeper (positive) regression slopes of calcium event rate vs. animal speed than ocean cells (Fig. 3*D*). To quantify the difference in speed modulation in island cells vs. ocean cells, we developed a simple speed modulation calculation that is robust to nonlinear modulation relationships: if a cell had significantly more calcium events during fast movement (animal speed > 10 cm/s) than during slow movement (<5 cm/s, but >2 cm/s to filter out quiet awake behavior state), then it was said to be significantly speed modulated (*Materials and Methods*). We found that islands had significantly more speed-modulated cells (135/590 cells = 23%) than oceans (4/544 cells = 1%) ($P < 10^{-50}$, χ^2 test; Fig. 3*E*). This was true also for the grid cell subpopulations in both islands (19/64 cells = 30%) and oceans (0/59 cells = 0%) ($P = 5.3 \times 10^{-6}$, χ^2 test). Thus, although both islands and oceans of MEC contain grid cells, they are differently speed modulated.

Discussion

A controversy exists in the literature about whether grid cells in MECII are predominantly ocean (8) or island cells, or both (9). Although these studies succeed in simultaneous spatial characterization and morphological characterization of individual cells, there remain several limitations. First, to obtain mechanically

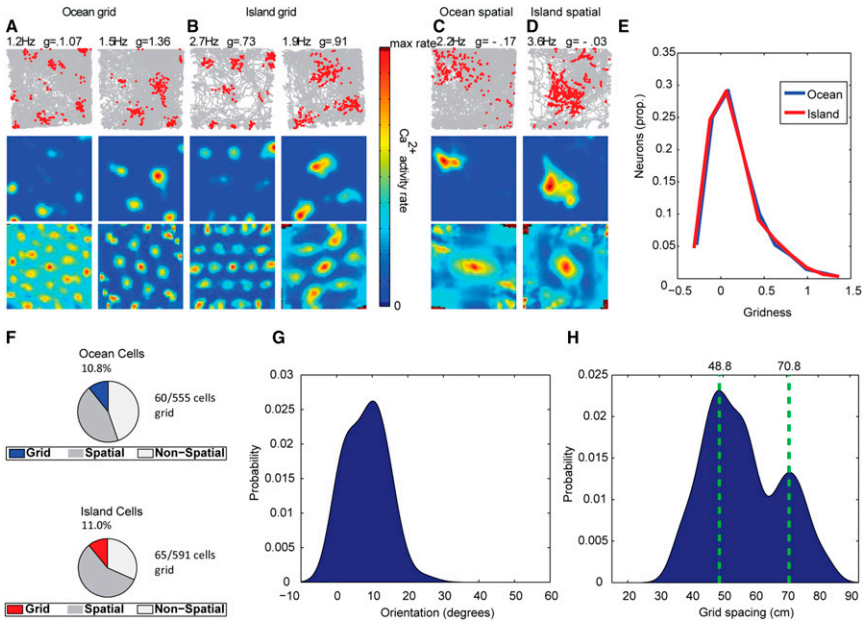

Fig. 2. Entorhinal oceans and islands both contain grid cells. (*A* and *B*) Two examples of ocean grid cells and two examples of island grid cells. Trajectory (gray) with calcium event positions (red) (first row), calcium event heat maps (second row), and spatial autocorrelograms (third row) in a 100 x 100-cm open field. Maximum Ca^{2+} event rate and gridness scores shown above figures. (*C* and *D*) One example of an ocean spatial cell and one example of an island spatial cell. (*E*) Distribution of grid scores in oceans and islands (n = 555 ocean cells; n = 591 island cells). (*F*) Percentage of grid cells in oceans and islands shown. (*G*) Distribution of grid orientation angles to the open-field border, mean angle at 8.27° (n = 62 grid cells). (*H*) Distribution of grid spacing. Peak spacings at 48.8 and 70.8 cm for a ratio of 1.45 (n = 62 grid cells).

stable whole-cell patch in vivo, a linear track behavior in virtual reality is often used instead of freely moving behaviors. Second, whole-cell patch and juxtacellular recordings in vivo are technically challenging recording techniques and unfortunately yield lower numbers of cells. Attempts have been made to use computational classifiers from these methods to try to classify cells from large-scale recordings (8) but remain indirect measures.

To address this controversy, we directly monitored the calcium activity of hundreds of entorhinal cells in a cell type-specific manner, in freely moving animals. Awake in vivo calcium imaging has been implemented previously in EC (16, 17), but thus far, only in head-fixed virtual linear track systems, without identification of neural type. We overcame the technical difficulty of directly and separately monitoring the activity of island and ocean cells from freely behaving mice in a 2D open space by combining a cell type-specific GCaMP-labeling method with the use of a miniaturized endoscope. This technique has recently been successfully implemented in other deep-brain structures such as the hypothalamus (18, 19), and in the hippocampus (11). Our implant followed the transverse fissure to minimize damage, and although there was damage in the cortex overlying the MEC, we detected no inflammation reaction in the area (Fig. 1 *J* and *K*). We were able to record from ocean and island cells that had calcium activity in a spatially periodic pattern during behavior, whose spatial period varied discretely (ratio = 1.45), and oriented 8.27° to the borders of the open field, which recapitulate known properties of grid cells (12–14). Overall, 11% of all cells recorded from dorsal MEC showed statistically significant grid activity, a percentage that corresponds well to the recent literature estimates in mice (ref. 8 showed ∼11% grid cells, and ref. 20 showed ∼15% grid cells). Through the large scale (n = 1146 cells in total) endoscopic monitoring, we show that grid cells (n = 125/1,146 cells in total) in dorsal MECII exist in comparable proportions in both the DG/CA3-projecting ocean and CA1-projecting island cell populations.

Prior electrophysiological recordings had suggested that grid cell activity is generally modulated by speed (4, 15). However, our results show this is much stronger for a specific subpopulation of grid cells, those within islands. Moreover, by comparison, DG and CA3-projecting ocean cells are much less modulated by an animal's current speed. The fact that island cells are more theta modulated than ocean cells (6) may be another aspect of island cells being more speed modulated than ocean cells, because theta has a close relation to animal moving speed (21, 22). Crucially, our implant methodology has no damage to cholinergic inputs to MEC (Fig. S3), which are important for the generation of these theta oscillations (23, 24). Thus, although both islands and oceans of MEC contain grid cells and other spatial cells, island cells are more active during increased animal movement speed, whereas only a very small percentage (1%; Fig. 3*E*) of ocean cells behaves that way.

Beyond the grid cell subpopulation, CA1-projecting island cells as a whole appear more intimately related to an animal's current locomotor state. In fact, island cells make up 95% of the ∼10% of MECII excitatory cells that show significant speed modulation according to our calculations. Downstream of island cells, CA1 cells fire more while the animal moves fast (25), and so island cells may be one source of speed-modulated information to CA1.

Animals keeps track of their spatial position by integrating self-motion information, a process called "path integration" (26, 27). In theoretical models of place representations, speed information is used for spatial updating in path integration computations (27–29). We speculate that island cells provide speed-modulated information to downstream path integration. Path integration computation may occur downstream in hippocampal circuits (27, 28), but it is more likely to occur in entorhinal circuits (30–32). If the latter mechanism is the case, one would expect island cell projections to other entorhinal circuits. Indeed, entorhinal island cells project to the contralateral MEC superficial layers (figure S5 of ref. 5). On the other hand, ocean cells are much less modulated by an animal's movement speed. DG and CA3, downstream of ocean cells, are important for contextual learning (33–36), and

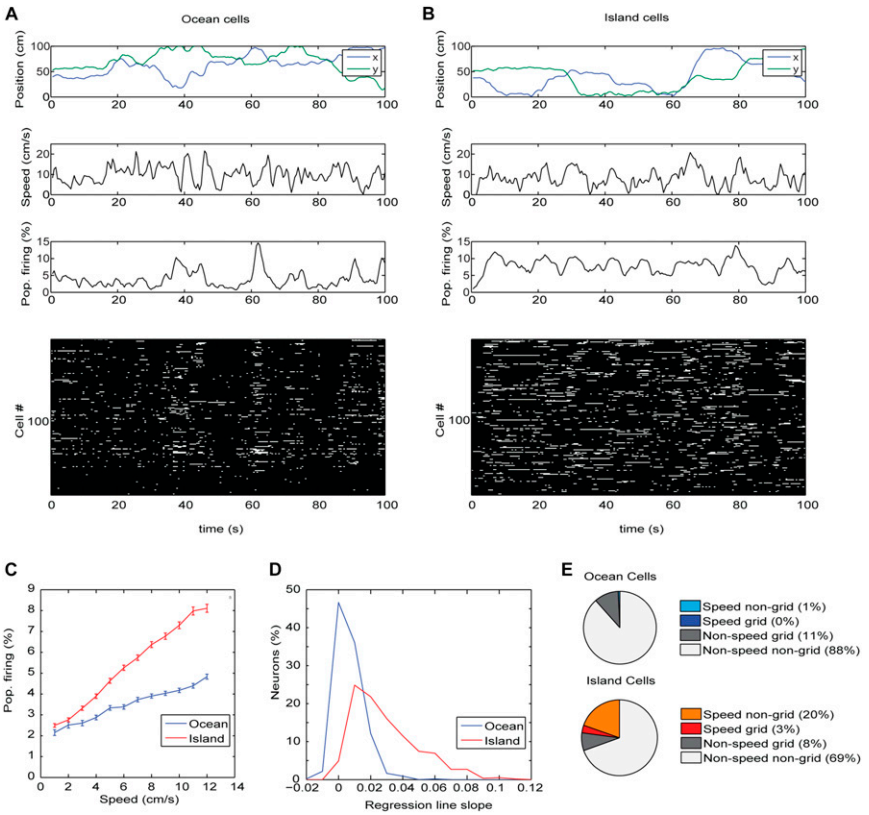

Fig. 3. Island cells are more speed modulated than ocean cells. (*A* and *B*) Two example behavior sessions: each showing the movement of the animal over time (top two rows, showing running position and running speed) compared with the population activity of either ocean cells (*A*) or island cells (*B*) over time (bottom two rows, showing percentage of cells firing, and calcium activity raster plot). (*C*) Mean percentage of neurons firing at different running speeds, across all animals, for island and ocean. Data are represented as mean ± SEM. (*D*) Distribution of regression line slopes for individual ocean and island cells. (*E*) Percentage of single cells in oceans and islands that are significantly speed modulated (n = 544 ocean cells; n = 590 island cells).

the ocean cell activity patterns may be well suited as an input for this function. We speculate that the entorhinal islands and oceans, despite both possessing spatially modulated cells such as grid cells, are differently speed modulated to subserve different downstream functions: island cells may contribute more to spatial path integration, whereas ocean cells may facilitate contextual representation in downstream circuits.

Materials and Methods

Animals. All procedures relating to mouse care and treatment conformed to Massachusetts Institute of Technology's Committee on Animal Care (CAC) and NIH guidelines. Animals were individually housed in a 12-h light (7:00 AM to 7:00 PM)/dark cycle. For studies of Ocean-GCaMP6f mice, we used WT male C57BL/6 mice, adults aged 36, 36, and 36 wk at the time of imaging. For studies of Island-GCaMP6f mice, we used the previously developed Wfs1-Cre transgenic male mice [Kitamura et al. (5)] maintained in the C57BL/6 background (Jackson Lab; main RBRC03751), adults aged 24, 36, and 56 wk at the time of imaging.

Histology and Immunohistochemistry. Mice were transcardially perfused with 4% (vol/vol) paraformaldehyde in PBS. Brains were then postfixed with the same solution for 24 h, and brains were sectioned by using a vibratome. For immunohistochemistory (IHC), sliced tissue sections were incubated in 0.3% Triton-X PBS with 5% (vol/vol) normal goat serum (NGS) for 1 h. Primary antibodies were then added to a 5% (vol/vol) NGS, 0.3% Triton X in PBS solution and incubated overnight at 4 °C. Primary antibodies were as follows: WFS-1 (Proteintech Group; 11558-1-AP; 1:500), CalbindinD-28K (Abcam; ab11426; 1:1,000) (SWANT; 300; 1:1,000), Reelin (MBL International; D223-3; 1:250), ionized calcium binding adaptor molecule 1 (Iba1) (Wako; 019-19741; 1000), NeuN (Millipore; MAB377; 1,000), and vesicular acetylcholine transporter (vChAT) (Frontier Institute; VAChT-Rb-Af1000-1; 1,000). After rinsing with PBS three times for 15 min each, sliced tissue sections were subsequently incubated with Alexa Fluor 405-, Alexa Fluor 488-, Alexa Fluor 546-, or Alexa Fluor 633-conjugated secondary antibodies (Invitrogen; 1:500). Sliced tissue sections were then washed in PBS three times for 15 min and mounted in VECTASHIELD medium on glass slides. Some sections were stained by DAPI or Nissl (1:500). Acetylcholinesterase (AChE) staining was performed by acetylcholinesterase rapid staining kit (MBL International). The IHC was not performed on GCaMP6f signal from AAV2/5-Syn-GCaMP6f or AAV2/5-Syn-DIO-GCaMP6f.

Preparation of AAV. The AAV2/5-Syn-DIO-GCaMP6f was generated by and acquired from the University of Pennsylvania Vector Core, with a titer of 1.3×10^{13} genome copy per mL. The AAV2/5-Syn-GCaMP6f was generated by and acquired from the University of Pennsylvania Vector Core, with a titer of 1.5×10^{13} genome copy per mL.

Stereotaxic Surgery. Stereotactic viral injections and microendoscope implantations were all performed in accordance with Massachusetts Institute of Technology's Committee on Animal Care guidelines. Mice were anesthetized using 500 mg/kg Avertin. Viruses were injected by using a glass micropipette attached to a 10-μL Hamilton microsyringe through a microelectrode holder filled with mineral oil. A microsyringe pump and its controller were used to control the speed of the injection. The needle was slowly lowered to the target site and remained for 10 min after the injection. For virus injections of island cells, unilateral viral delivery into the right MEC of the Wfs1-Cre mice was aimed at coordinates relative to bregma: anteroposterior (AP), −4.7 mm; mediolateral (ML), +3.35 mm; dorsoventral (DV), −3.30 mm. Wfs1-Cre mice were injected with 200 nL of AAV2/5-Syn-DIO-GCaMP6f. One month after injection, microendoscopes were implanted into the dorsal part of MEC of the Wfs1-Cre mice aimed at coordinates relative to bregma: AP, −5.1 mm; ML, ±3.36 mm; DV, −2.50 mm. For virus injections of ocean cells, unilateral viral delivery into the right DG of the WT mice was aimed at coordinates relative to bregma: AP, −2.0 mm; ML, +1.3 mm; DV, −2.05 mm. WT mice were injected with 150 nL of AAV2/5-Syn-GCaMP6f. One month after injection, we implanted (direct implant; no suction) microendoscope probes (1-mm diameter) into

the dorsal part of the WT mice aimed at coordinates relative to bregma: AP, −5.1 mm; ML, ±3.36 mm; DV, −2.50 mm. The probe was targeted to dorsal MEC while avoiding the transverse sinus, following the transverse fissure to reduce damage to the overlying cortices (Fig. S2).

One month after the implantation, the base plate for miniaturized microscope camera was attached above the implanted microendoscope in the mice. After experiments, all animals were perfused, and post hoc analyses were examined to determine actual imaging position in MEC of all animals (Fig. S2).

Behavior and Imaging. All behavior experiments took place during the animals' dark cycle. Island and ocean mice were habituated to human experimenters as well as the experimental room for 3 wk following implant surgeries. Open-field runs were done in a random order on a 100 × 100-cm dulled black surfaced open field without walls under dim light, with prominent visual cues within 50 cm on all sides of the box. The open field was raised 50 cm from the ground and had no walls. Ca^{2+} imaging in the open field lasted 60–100 min to collect a sufficient number of Ca^{2+} transients to power our statistical analyses. The open-field surface was cleaned between sessions. Immediately before and after imaging sessions, the mouse rested on a pedestal next to the open field.

Behavioral Analysis and Ca^{2+} Events Detection. The animal's position was captured by a camera via infrared light-emitting diodes (LEDs) attached to the animal. Calcium event maps were made on this high-resolution spatial map, whereas event rate HEAT maps were made by computationally binning the behavioral arena into 50 × 50 array of bins, each of which covered a 2 × 2-cm area. Smoothed rate maps were constructed with each pixel boxcar averaged over the surrounding 5 × 5 pixels with a Gaussian smoothing kernel $\sigma = 2$ pixels.

For presentation purposes (Fig. 2 and Figs. S4 and S5), smoothed rate maps were constructed with each pixel boxcar averaged over the surrounding 10 × 10 pixels with a Gaussian smoothing kernel $\sigma = 2$ pixels.

Calcium events were captured at 20 Hz on an Inscopix miniature microscope, time stamped to the start of the behavioral recording by the turning on of an LED that is fixed to the animal, at the beginning of the session, and turning off of the LED at the end. The calcium movie was then motion corrected in Inscopix Mosaic software. The Mosaic software parameters used for motion correction were as follows: correction type: translation and rotation; reference region with spatial mean ($r = 20$ pixels) subtracted, inverted, and spatial mean applied ($r = 5$ pixels). Finally, it was processed by custom-made code written in ImageJ [dividing each image, pixel by pixel, by a low-passed ($r = 20$ pixels) filtered version], a $\Delta F/F$ signal was calculated, and a spatial mean filter was applied to it in Inscopix Mosaic (disk radius = 3).

Two hundred cell locations were carefully selected from the resulting movie by principal component analysis–independent component analysis (PCA-ICA) [300 output principal components, 200 independent components (ICs), 0.1 weight of temporal information in spatiotemporal ICA, 750 iterations maximum, 1E-5 fractional change to end iterations] in Inscopix Mosaic software, and the ICs were binarized with a threshold equal to one-half of the maximum intensity. Regions of interest (ROIs) were constructed very small to minimize overlap between ROIs, with width equal to one-half the width of the binarized ICs. ROIs that were too elongated (if its length exceeded its width by more than two times) were discarded.

Fig. S7 visualizes these ROIs captured from the ICs for one example ocean mouse and one example island mouse.

Calcium traces were calculated at these ROIs for each processed movie, in ImageJ. Calcium events were detected by thresholding (>3 SDs from the $\Delta F/F$ signal) at the local maxima of the $\Delta F/F$ signal.

Gridness Score Calculation. Gridness scores were calculated for all cells that had more than 100 events while the animal moved at >2 cm/s.

For each cell, gridness was calculated from the spatial autocorrelogram, which was calculated based on Pearson's product-moment criterion applied to the smoothed rate map (defined above):

$$r(\tau_x,\tau_y)=\frac{n\Sigma\lambda(x,y)\lambda(x-\tau_x,y-\tau_y)-\Sigma\lambda(x,y)\Sigma\lambda(x-\tau_x,y-\tau_y)}{\sqrt{n\Sigma\lambda(x,y)^2-\left(\Sigma\lambda(x,y)\right)^2}\sqrt{n\Sigma\lambda(x-\tau_x,y-\tau_y)^2-\left(\Sigma\lambda(x-\tau_x,y-\tau_y)\right)^2}},$$

where $\lambda(x,y)$ is the average rate of a cell at location (x,y), and $r(\tau_x,\tau_y)$ is the autocorrelation between the fields with spatial lags of τ_x and τ_y. The summation is over n pixels in $\lambda(x,y)$ for which Ca^{2+} event rate was defined for both $\lambda(x,y)$ and $\lambda(x-\tau_x,y-\tau_y)$.

The central peak was cut out from the autocorrelogram. A series of circular masks in unitary increments from 8 pixels bigger than the central peak to 8 pixels smaller than the edge of the autocorrelogram was made. The Pearson coefficient was calculated between the mask and its 60° and 120° rotations on one side, and the mask and 30°, 90°, and 150° rotations on the other. A score was calculated based on the difference between the average of the two groups. The gridness score was defined as the maximum of these score, across all masks. All cells' calcium event times were shuffled 50 times according to Langston et al. (37) for a total of ∼10,000 shuffles per animal. Significant gridness scores were determined above the 95th percentile of all shuffles for each animal.

Grid Spacing. Analysis of grid spacing closely followed that of Stensola et al. (12). Individual fields were defined in the spatial autocorrelogram as neighboring bins with correlation above a set criterion (one-quarter of the maximum correlation). From the center field of the autocorrelogram, the three closest fields defined three axes for further analyses. Grid cells in which the minimal interaxis angle was smaller than 30° or exceeded 90°, or the grid spacing between pairs of axes exceeded a ratio of 2, were discarded. Grid scale was expressed as the arithmetic mean from the centers of mass of the three closest fields, to the center field.

Grid Orientation. Analysis of grid orientation closely followed Stensola et al. (13). Individual fields were defined in the spatial autocorrelogram as neighboring bins with correlation above a set criterion (one-quarter of the maximum correlation). From the center field of the autocorrelogram, the three closest fields defined three axes for further analyses. Grid cells in which the minimal interaxis angle was smaller than 30° or exceeded 90°, or the grid spacing between pairs of axes exceeded a ratio of 2, were discarded. For each cell, for each of the three axes, the angle to the nearest wall (in degrees) was calculated as follows:

$$A = 45 - abs([X \bmod 90] - 45),$$

where A is the angle of the axis to the nearest wall, and X is the angle of axis to an arbitrary wall.

The grid orientation was defined as the minimum offset (A_{min}) across the three axes, for each cell.

Kernel Density Estimate. Analysis of kernel smoothed density estimates of grid orientation and spacing closely followed Stensola et al. (12): 100 points equally spaced were used to cover the range of data, and the function

$$f(x)=\frac{1}{n}\sum_{i=1}^{n}K(x-x_i)$$

was defined where $x_1, \ldots x_n$ are the samples, and K is a Gaussian kernel with bandwidth σ.

Spatial Information. The tracked positions were sorted into 5 × 5-cm spatial bins, and the calcium event rate of each entorhinal cell was determined for each bin. The bins that had animal occupancy <50 ms were considered unreliable and discarded from further analysis. Without smoothing, the spatial information rate in bits per second was calculated for each cell according to the following:

$$\text{Information rate} = \sum_i p_i\lambda_i \log_2\frac{\lambda_i}{\lambda},$$

where λ_i is the mean calcium event rate of a unit in the ith bin, λ is the overall calcium event rate, and p_i is the probability of the animal occupying the ith bin for all i. All cells' event times were shuffled 50 times according to Langston et al. (37). Cells with significant spatial information were determined above the 95th percentile of all shuffles for each animal.

Cell Population Speed Modulation. The first 40,000 frames of each behavior session, sampled at 20 Hz, were taken to analyze speed modulation of cell activity, so that each animal was analyzed for the same behavioral time. Animal speed vs. population activity correlation was calculated for each recording session, which was binned into time bins of 500 ms that recorded whether a calcium event occurred or not. Population activity, defined as the percentage of active cells out of total cells at every time bin, was calculated, and average speed during each time bin was calculated for each animal.

Each animal's speed time series was normalized by its mean speed and SD. Each animal's population activity time series was normalized by its mean population activity and SD. On the one hand, all three ocean animals' normalized speed time series were amalgamated together as a long time series

to yield a long time series T_o, and all three ocean animals' normalized population activity time series were amalgamated together as a long time series to yield a long time series P_o. A Pearson correlation coefficient ρ_o was calculated between these amalgamated series. On the other hand, all three island animals' speed activity time series were amalgamated together as a long time series to yield a long time series T_i, and all three island animals' population activity time series were amalgamated together as a long time series to yield a long time series P_i. A Pearson correlation coefficient ρ_i was calculated between these amalgamated series. Finally, ρ_o and ρ_i were compared for ocean vs. island to quantify how their speed modulation differ.

To visualize these correlations in islands and oceans, the series T_o vs. P_o and T_i vs. P_i were used to plot ocean and island respectively, in Fig. S6.

Correlation of Instantaneous Cell Calcium Event Rate vs. Animal Speed. The instantaneous rate of calcium event of each individual cell was determined from the number of calcium transients that occurred in the 1-s time window place symmetrically around that time bin (time bins sampled at 20 Hz, as stated before). Linear regression analysis was performed on the instantaneous calcium event rate vs. the animal running speed for each individual cell, to yield the distribution of regression slopes (Fig. 3*C*).

Individual Cell Speed Modulation. The criteria to determine whether a single cell was "significantly speed modulated" was the following: "slow" movement was defined as animal running <5 cm/s (but >2 cm/s to filter out quiet awake behavior state). "Fast" movement was defined as the animal running >10 cm/s. One hundred events were randomly chosen from the set of Ca^{2+} events of the given cell, the speed at which the animal was running during the occurrence of this calcium event, was recorded, and the number of events occurring at fast and slow movement was determined. To compare the speeds during spiking to the speed statistics of the animal's behavior, we next picked 100 500-ms random time intervals from the behavioral experiment. The speed at which the animal was running during the occurrence of this event was recorded, and the amount of time spent at fast and slow movement was determined. This entire procedure was repeated 500 times for each cell, and an average number of events at fast and slow movement, and time in fast and slow movement was calculated.

Based on these averages, we compared the following proportions:

$$\frac{n_{\text{fast}}}{n_{\text{total}}} \text{ vs. } \frac{t_{\text{fast}}}{t_{\text{total}}},$$

where n_x is the average number of calcium events in category x, and $n_{\text{total}} = n_{\text{slow}} + n_{\text{fast}}$, and t_x is the amount of time the animal spent in category x, and $t_{\text{total}} = t_{\text{slow}} + t_{\text{fast}}$.

A cell was significantly speed modulated if it had significantly more calcium events per unit time spent in fast movement than in slow movement (i.e., $n_{\text{fast}}/n_{\text{total}}$ is significantly different from and greater than $t_{\text{fast}}/t_{\text{total}}$, as determined by a χ^2 test, $P < 0.05$, with Bonferroni correction).

To visualize the speed modulation between island and ocean cells as defined in this way, we calculated a "speed modulation index" for each individual cell in the following way:

$$\text{Index} = \frac{\frac{n_{\text{fast}}}{n_{\text{total}}}}{\frac{t_{\text{fast}}}{t_{\text{total}}}},$$

The index takes the propensity of the cell to be active during "fast" movement and normalizes it to the proportion of time the animal spends during "fast." We presented the distribution of speed indices in Fig. S8 for island and ocean cells.

ACKNOWLEDGMENTS. We thank J. Z. Young and H. Eichenbaum for discussions; A. Hamalian, C. Ragion, L. Smith, M. Ragion, S. Perry, and W. Yu for experimental help; P. Jercog, D. Roy, and C. MacDonald for paper comments; L. Brenner for paper preparation; and the members of S.T. laboratory for their support. This work was supported by the RIKEN Brain Science Institute (S.T.), the Picower Institute Innovation Fund (S.T.), and the JPB Foundation (T.K.). L.J.K. was supported by a National Science Foundation graduate fellowship.

1. O'Keefe J, Nadel L (1978) *The Hippocampus as a Cognitive Map* (Oxford Univ Press, Oxford).
2. Morris RGM, Garrud P, Rawlins JNP, O'Keefe J (1982) Place navigation impaired in rats with hippocampal lesions. *Nature* 297(5868):681–683.
3. Hafting T, Fyhn M, Molden S, Moser M-B, Moser EI (2005) Microstructure of a spatial map in the entorhinal cortex. *Nature* 436(7052):801–806.
4. Sargolini F, et al. (2006) Conjunctive representation of position, direction, and velocity in entorhinal cortex. *Science* 312(5774):758–762.
5. Kitamura T, et al. (2014) Island cells control temporal association memory. *Science* 343(6173):896–901.
6. Ray S, et al. (2014) Grid-layout and theta-modulation of layer 2 pyramidal neurons in medial entorhinal cortex. *Science* 343(6173):891–896.
7. Varga C, Lee SY, Soltesz I (2010) Target-selective GABAergic control of entorhinal cortex output. *Nat Neurosci* 13(7):822–824.
8. Tang Q, et al. (2014) Pyramidal and stellate cell specificity of grid and border representations in layer 2 of medial entorhinal cortex. *Neuron* 84(6):1191–1197.
9. Domnisoru C, Kinkhabwala AA, Tank DW (2013) Membrane potential dynamics of grid cells. *Nature* 495(7440):199–204.
10. Chen T-W, et al. (2013) Ultrasensitive fluorescent proteins for imaging neuronal activity. *Nature* 499(7458):295–300.
11. Ziv Y, et al. (2013) Long-term dynamics of CA1 hippocampal place codes. *Nat Neurosci* 16(3):264–266.
12. Stensola H, et al. (2012) The entorhinal grid map is discretized. *Nature* 492(7427): 72–78.
13. Stensola T, Stensola H, Moser M-B, Moser EI (2015) Shearing-induced asymmetry in entorhinal grid cells. *Nature* 518(7538):207–212.
14. Krupic J, Bauza M, Burton S, Barry C, O'Keefe J (2015) Grid cell symmetry is shaped by environmental geometry. *Nature* 518(7538):232–235.
15. Wills TJ, Barry C, Cacucci F (2012) The abrupt development of adult-like grid cell firing in the medial entorhinal cortex. *Front Neural Circuits* 6:21.
16. Heys JG, Rangarajan KV, Dombeck DA (2014) The functional micro-organization of grid cells revealed by cellular-resolution imaging. *Neuron* 84(5):1079–1090.
17. Low RJ, Gu Y, Tank DW (2014) Cellular resolution optical access to brain regions in fissures: Imaging medial prefrontal cortex and grid cells in entorhinal cortex. *Proc Natl Acad Sci USA* 111(52):18739–18744.
18. Betley JN, et al. (2015) Neurons for hunger and thirst transmit a negative-valence teaching signal. *Nature* 521(7551):180–185.
19. Jennings JH, et al. (2015) Visualizing hypothalamic network dynamics for appetitive and consummatory behaviors. *Cell* 160(3):516–527.
20. Giocomo LM, et al. (2011) Grid cells use HCN1 channels for spatial scaling. *Cell* 147(5): 1159–1170.
21. Jeewajee A, Barry C, O'Keefe J, Burgess N (2008) Grid cells and theta as oscillatory interference: Electrophysiological data from freely moving rats. *Hippocampus* 18(12): 1175–1185.
22. Hinman JR, Penley SC, Long LL, Escabí MA, Chrobak JJ (2011) Septotemporal variation in dynamics of theta: Speed and habituation. *J Neurophysiol* 105(6):2675–2686.
23. Mitchell SJ, Rawlins JN, Steward O, Olton DS (1982) Medial septal area lesions disrupt theta rhythm and cholinergic staining in medial entorhinal cortex and produce impaired radial arm maze behavior in rats. *J Neurosci* 2(3):292–302.
24. Jeffery KJ, Donnett JG, O'Keefe J (1995) Medial septal control of theta-correlated unit firing in the entorhinal cortex of awake rats. *Neuroreport* 6(16):2166–2170.
25. Zheng C, Bieri KW, Trettel SG, Colgin LL (January 20, 2015) The relationship between gamma frequency and running speed differs for slow and fast gamma rhythms in freely behaving rats. *Hippocampus*, 10.1002/hipo.22415.
26. Darwin C (1873) Origin of certain instincts. *Nature* 7:417–418.
27. McNaughton BL, et al. (1996) Deciphering the hippocampal polyglot: The hippocampus as a path integration system. *J Exp Biol* 199(Pt 1):173–185.
28. Samsonovich A, McNaughton BL (1997) Path integration and cognitive mapping in a continuous attractor neural network model. *J Neurosci* 17(15):5900–5920.
29. O'Keefe J, Burgess N (2005) Dual phase and rate coding in hippocampal place cells: Theoretical significance and relationship to entorhinal grid cells. *Hippocampus* 15(7): 853–866.
30. Burak Y, Fiete IR (2009) Accurate path integration in continuous attractor network models of grid cells. *PLoS Comput Biol* 5(2):e1000291.
31. Fuhs MC, Touretzky DS (2006) A spin glass model of path integration in rat medial entorhinal cortex. *J Neurosci* 26(16):4266–4276.
32. McNaughton BL, Battaglia FP, Jensen O, Moser EI, Moser M-B (2006) Path integration and the neural basis of the "cognitive map." *Nat Rev Neurosci* 7(8):663–678.
33. McHugh TJ, et al. (2007) Dentate gyrus NMDA receptors mediate rapid pattern separation in the hippocampal network. *Science* 317(5834):94–99.
34. Nakashiba T, et al. (2012) Young dentate granule cells mediate pattern separation, whereas old granule cells facilitate pattern completion. *Cell* 149(1):188–201.
35. Nakazawa K, et al. (2002) Requirement for hippocampal CA3 NMDA receptors in associative memory recall. *Science* 297(5579):211–218.
36. Nakashiba T, Young JZ, McHugh TJ, Buhl DL, Tonegawa S (2008) Transgenic inhibition of synaptic transmission reveals role of CA3 output in hippocampal learning. *Science* 319(5867):1260–1264.
37. Langston RF, et al. (2010) Development of the Spatial Representation System in the Rat. *Science* 328(5985):1576–1580.